

# Giving Cosmic Redshift Drift a Whirl

Alex G. Kim<sup>1</sup>, Eric V. Linder<sup>1,2</sup>, Jerry Edelstein<sup>2</sup>, David Erskine<sup>3</sup>

## ABSTRACT

Redshift drift provides a direct kinematic measurement of cosmic acceleration but it occurs with a characteristic time scale of a Hubble time. Thus redshift observations with a challenging precision of  $10^{-9}$  require a 10 year time span to obtain a signal-to-noise of 1. We discuss theoretical and experimental approaches to address this challenge, potentially requiring less observer time and having greater immunity to common systematics. On the theoretical side we explore allowing the universe, rather than the observer, to provide long time spans; speculative methods include radial baryon acoustic oscillations, cosmic pulsars, and strongly lensed quasars. On the experimental side, we explore beating down the redshift precision using differential interferometric techniques, including externally dispersed interferometers and spatial heterodyne spectroscopy. Low-redshift emission line galaxies are identified as having high cosmology leverage and systematics control, with an 8 hour exposure on a 10-meter telescope (1000 hours of exposure on a 40-meter telescope) potentially capable of measuring the redshift of a galaxy to a precision of  $2 \times 10^{-9}$  ( $\sim 5 \times 10^{-11}$ ). Low-redshift redshift drift also has very strong complementarity with cosmic microwave background measurements, with the combination achieving a dark energy figure of merit of nearly 300 (1400) for 5% (1%) precision on drift.

*Subject headings:* cosmological distances; cosmic acceleration; dark energy

## 1. Introduction

Our universe is dynamic, i.e. the metric evolves, or more simply the scale factor of the universe changes with time: hence  $a(t)$ . This gives rise to the cosmic redshift of light from distant sources. Moreover, since the expansion rate itself evolves, in all but a coasting, Milne universe, the redshift of an object with fixed comoving coordinate will shift. This redshift drift was introduced by Sandage (Sandage 1962) and McVittie (McVittie 1962) in the early 1960s and revisited in the 1980s and 1990s; see the textbook summary in Linder (1997).

Just as redshift is direct, kinematical evidence for cosmic expansion, redshift drift is likewise for cosmic acceleration. This directness is an attrac-

tive feature as it does not depend on dynamics, i.e. the equations of motion (and separation of matter and dark energy density). So even if such a cosmic probe cannot reach the accuracy of, say, distance or growth of structure probes on dynamical cosmological-model parameters, it is worthwhile exploring possibilities for carrying it out.

Conventionally, this is thought of in a brute force approach: stare at an object for a long time and measure the change in its redshift. Since the time scale for an order unity variation is the characteristic time scale of the expansion, the Hubble time of  $\sim 10^{10}$  y, this requires fantastically precise measurements of redshift stable over the observing period. Moreover, any other time variation in the metric that is not linear gives a competing effect. From the Principle of Equivalence, any acceleration of the source or change in gravity along the line of sight acts as a systematic contribution.

Here we explore two parallel tracks to make this cosmological probe more viable. One is exploring theoretical ideas for letting the universe do

<sup>1</sup> Physics Division, Lawrence Berkeley National Laboratory, 1 Cyclotron Road, Berkeley, CA, 94720, USA

<sup>2</sup> Space Sciences Laboratory, University of California Berkeley, 7 Gauss Way, Berkeley, CA 94720, USA

<sup>3</sup> Lawrence Livermore National Laboratory, Livermore, CA 94550, USA

the difficult work for us, by taking advantage of source redshifts delivered to us at effectively different epochs and of differential rather than absolute measurements. The second involves experimental approaches to improve the brute force precision, while again using differential measurements to ameliorate instrumental systematics. As with any probe, systematics are a key concern so any method that may enable better control of them is important to consider.

In Sec. 2 we review the basic redshift drift and the plethora of systematics that confront it, as well as the potential leverage on cosmological model parameters. Section 3 outlines three theoretical alternatives to the brute force approach, each with their own advantages and speculative aspects. We turn to some innovative experimental approaches in Sec. 4, which may offer improvements in precision and systematics, and conclude in Sec. 5.

## 2. Redshift Drift and Systematics

In back-to-back articles published in 1962, McVittie (1962) and Sandage (1962) laid out the basics of redshift drift. Since the cosmic redshift  $z = a^{-1} - 1$ , then the dependence  $a(t)$  of the source with respect to the observer necessarily implies that  $z$  changes with time as well. Following the approach in Linder (1997), we have

$$\begin{aligned} \frac{dz}{dt_0} &= \frac{d}{dt_0} \left[ \frac{a(t_0)}{a(t_e)} - 1 \right] = \frac{\dot{a}(t_0) - \dot{a}(t_e)}{a(t_e)} \quad (1) \\ &= (1+z)H_0 - H(z), \quad (2) \end{aligned}$$

where  $t_0$  is the time the signal is observed in the observer-frame,  $t_e$  the signal emission time, and  $H = \dot{a}/a$  the Hubble expansion rate. Note that a dot superscript denotes a derivative with respect to the time argument shown.

The form involving a difference between  $\dot{a}$ 's makes clear that this arises from acceleration (positive or negative). Only a universe where  $\dot{a} = \text{constant}$ , i.e.  $a \propto t$ , has no redshift drift. This is a Milne universe, which is conformal to a Minkowski spacetime, and so the Principle of Equivalence assures us that a universe without gravity has no acceleration, and vice versa. We emphasize the kinematic aspect of the redshift drift: its nonzero value at any redshift directly indicates acceleration, with no need to know the dynamics, i.e. the specific functional dependence  $a(t)$ . While

distance measurements are kinematic, they must be differenced or differentiated to reveal acceleration (ideally through a regression method, e.g. Shafieloo et al. (2012); Seikel et al. (2012)), or fit to a dynamical model (Riess et al. 1998; Perlmutter et al. 1999). Only when we want to compare to a particular model, e.g. so much matter density and so much dark energy density with some equation of state, do we need to know  $a(t)$ .

At high redshift we expect the universe to be decelerating, and hence the drift should be negative. When the universe begins to accelerate (speed up) under the influence of dark energy in recent times, however, then the drift will change to positive. Thus the hope is to map out the influence of dark energy, and its equation of state, by accurate measurements of the redshift drift (in addition to establishing directly the mere presence of positive acceleration).

Figure 1 shows the sensitivity of the drift  $\dot{z}$  as a function of source redshift to the cosmological parameters of the matter density  $\Omega_m$  and dark energy equation of state  $w(a) = w_0 + w_a(1 - a)$ , where  $w_0$  is its present value and  $w_a$  a measure of its time variation. The results use the fiducial values  $\Omega_m = 0.3$ ,  $w_0 = -1$ ,  $w_a = 0$  and the vertical scale is in units of  $H_0$ . In these units,  $\partial\dot{z}/\partial H_0$  is given by the  $\dot{z}$  curve. The key properties to notice are: 1) The sensitivity curves are different shapes, indicating no strong covariance between the effects of the different parameters, as long as measurements cover a range of redshifts, 2) The greatest sensitivity is to the matter density, and this continues to outweigh the equation of state parameters at higher redshifts, by ever increasing factors, and 3) The initial rise of the equation of state sensitivities is sharp, achieving 50% of the maximum sensitivity at quite low redshifts. These characteristics suggest that low-redshift measurements, especially if they have better signal to noise than higher redshift ones, could be valuable for cosmological leverage on dark energy through the redshift drift probe. We will see that this in fact fits in well with the new experimental techniques introduced in Sec. 4.

At low redshift  $\dot{z} \approx -H_0 q_0 z$  so the cosmological sensitivity initially increases linearly with redshift. If the precision is photon noise limited, then it will go inversely with the luminosity distance. Since luminosity distance grows initially linearly with

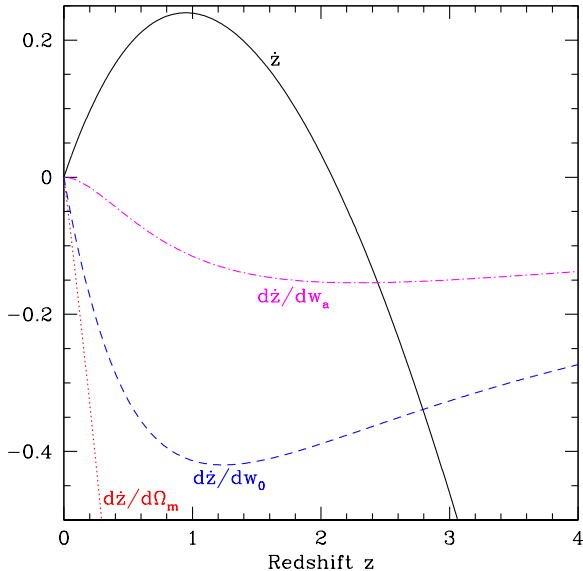


Fig. 1.— The dependence of the redshift drift  $\dot{z}$  and the sensitivities  $\partial\dot{z}/\partial p$  to various cosmological parameters  $p$  are shown as functions of redshift. All quantities are in units of  $H_0$ , hence the redshift drift over an observing time  $\Delta t$  is  $\Delta z \lesssim H_0 \Delta t = 10^{-10} h(\Delta t/y)$ .

redshift, then more quickly at higher redshift, this indicates that low redshift may give the strongest cosmological leverage.

Another consideration is that the low-redshift  $q_0$  dependence (which accords with redshift drift being a direct probe of acceleration) implies the sensitivity to  $\Omega_m$  will be a factor  $\sim 3/2$  better than to  $w_0$ , in agreement with Fig. 1. The sensitivity to matter density continues to increase with redshift, growing from linear with  $z$  to proportional to  $z^{3/2}$  at high redshift, swamping the dark energy parameters, whose sensitivities decline at high redshift. These characteristics give merit to further exploration of the use of low-redshift sources.

We can quantify the redshift range having optimal leverage on dark energy parameters  $w_0$  and  $w_a$ , and their figure of merit (FOM)  $[\det Cov(w_0, w_a)]^{-1/2}$  inversely proportional to the area of their joint uncertainty contour, through Fisher analysis using the sensitivities exhibited in Fig. 1.

Figure 2 shows the results for the illustrative case of five measurements of  $\dot{z}$  at 1% precision

each, centered on  $z$ , i.e. at redshifts  $z-0.2$ ,  $z-0.1$ ,  $z$ ,  $z+0.1$ ,  $z+0.2$ . We marginalize over  $\Omega_m$ , and over  $H_0$  with a prior of 0.03 (current precision) on  $h = H_0/(100 \text{ km s}^{-1} \text{ Mpc}^{-1})$ . As expected from our previous discussion, the parameters are best determined from low-redshift observations, despite that  $\dot{z}$  itself is largest at high redshift. This is due to a combination of dark energy being most prominent at low redshift, and that parameter covariances are smaller at low redshift. Note that near  $z = 2$ , when  $\dot{z} = 0$  and so there is also no sensitivity to  $H_0$ , the leverage temporarily increases due to relief from covariance with  $H_0$ . However by  $z \approx 2.4$  the figure of merit has declined by more than a factor 10 from its low-redshift peak. This low-redshift leverage is advantageous since the signal-to-noise of the measurements we discuss later is much better at low redshifts.

Figure 3 illustrates the joint dark energy constraints from measurements at low, medium, and high redshift ranges, marginalizing over  $\Omega_m$ , and over  $h$  with a prior of 0.03. A further virtue of the low-redshift redshift drift probe is the positive orientation of the joint confidence contour, highly complementary to the negative orientation of nearly all other cosmological probes such as distances. This complementarity is lost for higher redshifts. However, if feasible, redshift drift measurements at high *and* low redshifts have great synergy. For example, the constraint from adding the  $z = 2.8$  measurements to the  $z = 0.3$  measurements yields a figure of merit of 784, about 6.6 times higher than the  $z = 0.3$  case alone. Alternatively, if we move away from purely kinematic observations and include measurement of the distance to cosmic microwave background (CMB) last scattering by Planck, then we obtain even greater synergy with low redshift drift observations – a FOM of 1414, or 12 times higher than the  $z = 0.3$  case alone (also see the light grey FOM<sub>CMB</sub> curve in Figure 2). We have also investigated an alternate error model where instead of a constant fractional precision with redshift we have a constant absolute precision. This does not change the key aspect that low redshift still has the greatest leverage.

The key question, however, is how practical such measurements are, both with respect to needed precision and to systematic effects that degrade the accuracy. If the error floor lies at 5%

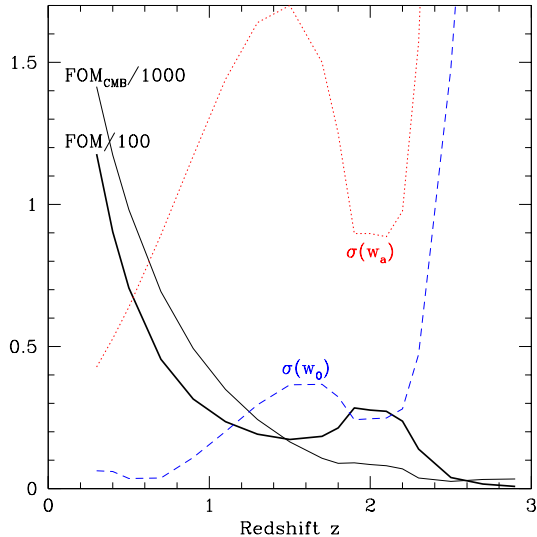


Fig. 2.— Constraints at  $1\sigma$  on  $w_0$  and  $w_a$ , and their joint figure of merit (FOM), are plotted vs central redshift for experiments consisting of five measurements of redshift drift at 1% precision. CMB constraints are included in (only) the  $FOM_{\text{CMB}}$  curve; note it is shown divided by 1000, rather than 100 like the FOM curve without CMB.

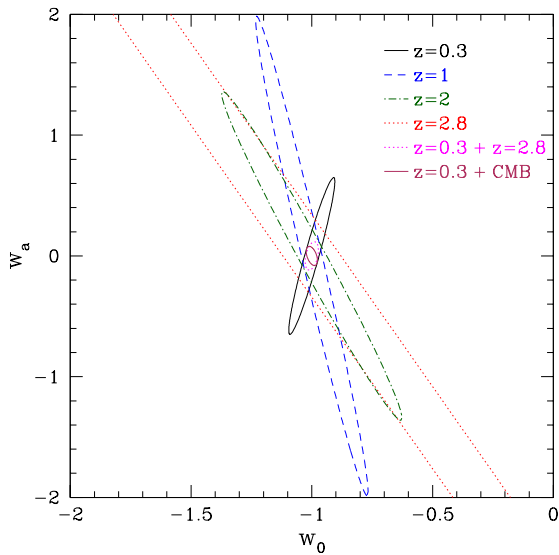


Fig. 3.— Joint constraints on the dark energy equation of state parameters  $w_0$  and  $w_a$  are shown at 68% confidence level, for experiments consisting of five measurements of redshift drift at 1% centered at redshift  $z$ .

rather than 1%, the  $z = 0.3$  case delivers only a figure of merit of 6.6, though the combined  $z = 0.3 + \text{CMB}$  case gives 289, showing the strong complementarity. Figure 4 depicts how the figure of merit depends on the drift measurement precision; it stays above 100 (“stage 3”) out to 10% precision. We also see that tightening the prior on  $h$  helps considerably in the strong precision case, improving FOM by a factor 1.65 to over 2300 when the prior goes from 0.03 to 0.01 (but for 5% precision the factor is 1.3).

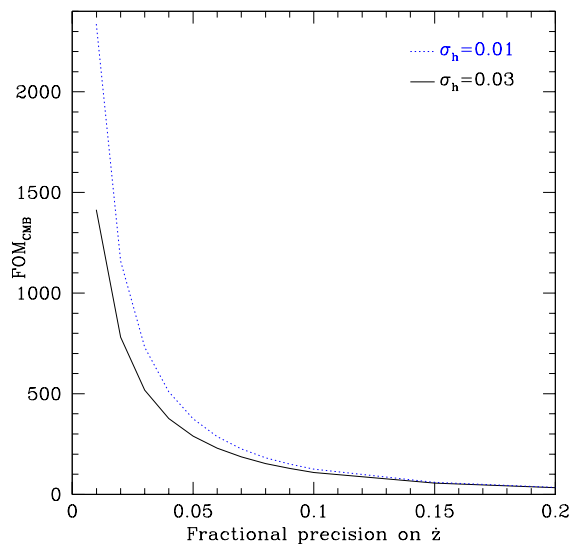


Fig. 4.— The dark energy figure of merit is plotted as a function of redshift drift measurement precision, for a combination of five measurements centered at  $z = 0.3$  plus Planck CMB last scattering distance. The blue dotted curve shows the effect of tightening the Hubble constant prior to 0.01.

We now outline some of the concerns regarding astrophysical systematic uncertainties. Sec. 4 will address improvements in precision and some experimental systematics using new experimental techniques.

One astrophysical fly in the ointment is that in fact the observed redshift  $z \neq a^{-1} - 1$ . The full relativistic expression is

$$1 + z = \frac{(g_{\mu\nu}k^\mu u^\nu)_e}{(g_{\mu\nu}k^\mu u^\nu)_o}, \quad (3)$$

with the redshift drift obtaining contributions from not only the homogeneous expansion in the

metric, but 1) inhomogeneous gravitational potentials, 2) deviations in the photon four-momentum  $k^\mu$  due to inhomogeneities, and 3) time variation of the source four-velocity  $u^\nu$ , i.e. peculiar accelerations.

The full expression for the redshift drift including metric and geodesic effects but not peculiar acceleration is

$$\begin{aligned} \frac{dz}{dt_o} = & \frac{\dot{a}_o - \dot{a}_e}{a_e} \quad (4) \\ & + 2[\dot{\psi}_e - (1+z)\dot{\psi}_o] + \frac{2}{a_e} \partial_1(\psi_e - \psi_o) \\ & - (\dot{\phi}_e - \dot{\phi}_e) + (1+z)(\dot{\psi}_o - \dot{\phi}_o) \\ & - H(z)(\phi_o - \phi_e) + H_0(1+z)[a_o k_o^0]^{(1)} , \end{aligned}$$

where  $\psi$  and  $\phi$  are the metric gravitational potentials. These terms are discussed in detail in Linder (2010); most are smaller than, though some are comparable to (especially for relativistic systems), peculiar accelerations.

As for peculiar accelerations, using  $\vec{\nabla}\psi \sim \dot{u}$ , the contribution is

$$\dot{u} \sim \frac{\psi}{L} \sim H \frac{H^{-1}}{L} \psi \sim H \left( \frac{40 \text{ kpc}}{L} \right) \left( \frac{\psi}{10^{-5}} \right) , \quad (5)$$

where  $L$  is a characteristic size of the system. This contribution can be the same order of magnitude as the first, McVittie-Sandage term, and so is not obviously negligible when talking about active galactic nuclei as sources, for example. It is crucial to realize that this should not be interpreted statistically, i.e. averaging over sources in low-density and high-density regions, but treated for an individual line of sight. Similarly it should not be treated as though the source was in the linear density perturbation regime.

Methods exist for ameliorating these systematics, e.g. observing several well separated sources. However the precision required for measurement of redshift drift at a signal-to-noise of merely unity is  $dz \approx 10^{-10}$  over a year (or  $10^{-9}$  over 10 years), so a 1% measurement would require  $dz \approx 10^{-12}$  over a year. Systematics would need to be reduced below these levels.

### 3. Speculative Shortcuts for the Impatient

Since the requirements on measuring  $dz$  are so challenging, concepts for observational probes that

inherently use long time scales or multiple measurements in one system to would be of particular interest. A long lever arm in time and many measurements could reduce the requirements on individual measurement precision. The universe itself provides sources at many different epochs, spread out over a Hubble time. Likewise, individual sources can provide many different signals, e.g. spectral lines or wavetrains. In this section we explore the use of each of these characteristics, and then their combination, in potential probes of acceleration. In general these either do not exactly give redshift drift, or are more speculative than established, so after this section we return to the stare-and-wait approach, but they are worth further consideration.

#### 3.1. Many sources: Radial baryon acoustic oscillations

While the light from sources at different redshifts reaches us after being emitted at vastly different times, this does not inform us regarding redshift drift that involves the change of a given source over time. However, we can still probe cosmic acceleration in a kinematic way through a related quantity, analogously called Hubble drift. This is how the Hubble parameter  $H(z)$  changes over redshift, rather than how redshift of a given source changes over time. But it can be measured kinematically and does give information on acceleration.

We can think of a statistical ensemble of objects collectively as a source, for example defining a baryon acoustic feature in the density power spectrum. This encodes a particular comoving scale, roughly the sound horizon  $s$  at baryon-photon decoupling. By measuring it along the line of sight, we are measuring a cosmic length  $dr \sim 150$  Mpc with endpoints at two different redshifts so  $dr = dz/H$ . Since  $dz \approx 0.05$  then  $H$  is fairly constant over this interval and we can simply say we obtain a measurement  $H(z_1)$ , where  $z_1$  is the mean redshift. This is called a radial baryon acoustic oscillation (BAO) measurement, of the quantity  $sH$ .

Carrying this out in a second redshift slice delivers  $H(z_2)$ . Propagating the errors from each we can create a differential radial BAO (drBAO) measurement

$$R = s(H_2 - H_1) . \quad (6)$$

For redshift differences not small compared to unity, we measure the Hubble expansion parameter at times separated by a substantial fraction of the Hubble time,  $\sim 10^{10}$  y. That is, we have left it to the universe to do the work of providing the long time baseline.

While drBAO gives the ‘‘Hubble drift’’ rather than the redshift drift (in particular we measure the change in Hubble parameter over redshift, not the change in redshift over time), these two quantities are closely related, and indeed the Hubble drift measurement has some useful differences as shown in Table 1. The nuisance parameter for comparing to cosmology theory is  $H_0$  for the redshift drift, while it is the much better known sound horizon  $s$  for drBAO. While redshift drift has a null at the acceleration-deceleration transition, drBAO has a null at the superacceleration or phantom transition, when the total equation of state of the universe  $w_{\text{tot}} = -1$ . Finally, spectroscopic galaxy surveys measuring BAO also provide drBAO so no separate instrument or experiment is required.

Probe	Quantity	Marg.	Sign Flip
$z$ drift	$(1+z)H_0 - H(z)$	$H_0$	$w_{\text{tot}} = -1/3$
drBAO	$s[H(z_2) - H(z_1)]$	$s$	$w_{\text{tot}} = -1$

Table 1: Redshift drift and differential radial BAO both directly measure the acceleration of the universe, but with different marginalization parameters and observational requirements.

### 3.2. Many signals: Cosmic pulsars

The long time baseline of the drBAO probe ameliorates the redshift precision needed, to simply that needed to measure the radial BAO scale ( $dz \approx 10^{-3}$ ). However it does involve the clustering of large scale structure and a statistical measure rather than simply photon propagation from an individual source. If a single source gave many measurements, i.e. emitted many signals each of which could be used to measure redshift drift, then the requirement on the redshift precision can also be ameliorated in this manner. Conventionally this is thought of in terms of many spectral lines; we return to this later but here explore the time domain.

If the source repeatedly emitted signals, then by measuring  $N$  of them we could hope to statistically reduce the uncertainty on the redshift drift.

Moreover, if there is a specific pattern to the signals, e.g. a periodicity, then further gains can be made. This is the idea behind the period probe, or cosmic pulsar test; here we follow the textbook treatment of Linder (1997). The time observed for the arrival of the  $N$ th pulse with initial emitted period  $P$  is

$$\begin{aligned}
 t_N &\equiv t_o(NP) \\
 &= NP \frac{dt_o}{dt_e} + \frac{1}{2} (NP)^2 \frac{d^2 t_o}{dt_e^2} + \dots \quad (7) \\
 &= NP(1+z) \\
 &\quad + \frac{1}{2} (NP)^2 (1+z) [(1+z)H_0 - H(z)] \quad (8)
 \end{aligned}$$

The redshift drift (in square brackets) is thus enhanced by  $N^2$  (that is, the precision on  $\dot{z}$  scales as  $N^{-2}$ ) and can be specifically fit to the quadratic behavior of the time series, helping to make a clean detection. There is an extensive literature on pulsar timing and efficient fitting of different contributions (Lorimer 2008).

While pulsars are fantastically regular clocks, well suited to this probe, we do not currently detect them at cosmological distances in the Hubble flow (but see Thornton et al. 2013). The idea behind cosmic pulsars is not restricted to neutron stars, however. One could consider other sources of (quasi-)periodic signals such as gravitational waves from supermassive binary black hole inspirals, which should be detectable at cosmic distances. An issue here (other than detecting such sources) is that in these systems redshift is not measured separately but is tied with the black hole masses into the chirp mass combination. Any evolution in the black hole masses – or Newton’s constant – would be a systematic; see the analysis in Appendix B of Yunes et al. (2010) following a suggestion by Linder. Finally, any other accelerations, such as the motion of the system through an inhomogeneous gravitational potential or pulsar or gravitational wave kicks, would be a systematic.

### 3.3. Multiple sources and signals: Strongly lensed quasars

The ideal situation would be to combine the long time baseline provided by cosmological distances as in the drBAO method with the multiple signals per source as in the cosmic pulsar method. While this cannot be exactly done, some of advan-

tages of each enter in the use of strongly lensed sources, plus the ability to do a differential rather than absolute measurement.

Strong gravitational lensing produces multiple images of the source, and so in a single system one can measure the redshift along multiple lines of sight. Gravitational lensing itself is achromatic in the geometric optics regime (wavelength divided by effective lens scale much less than one, an excellent approximation at ultraviolet and optical wavelengths) and so the redshifts will be the same.

Moreover, due to the different light paths there will be time delays between the spectra observed of each image. This is used in strong lensing as a cosmological distance probe itself (see, e.g., Treu et al. (2013) and references therein). Here, however, it provides a time baseline for the redshift drift of the individual source. If the time delay were of order 10 years (or even better a substantial fraction of the Hubble time) then the required redshift measurement precision would be eased, but observed systems have time delays of days to years (Fohlmeister et al. 2007, 2008, 2013). Still, the universe is giving us for free a time baseline of a year though the redshift observations may be done in a single night.

Note that unlike for time-delay distances we have no need to model the time delay through knowledge of the lens mass profile, image geometry, etc. – all we need to do is measure it from monitoring the light curves of the images. A bright, time varying source such as a quasar is ideal for this, and the time delay is measured from the photometric light curves (see, e.g. Tewes et al. (2013); Hojjati et al. (2013) for statistical techniques for robust estimation). Since we do not need to model the lens mass profile, we can use cluster lenses, with larger time delays, rather than restricting to galaxy lenses as for the time-delay distance technique.

If the lines of sight are within the spectrograph field of view, then they can be observed simultaneously, allowing a direct differential measurement to give the redshift drift, rather than an absolute one. Furthermore, this increases the likelihood that the Lyman- $\alpha$  absorption is coherent between the multiple lines of sight. The transverse distance at redshift  $z$  between lines of sight separated by

angle  $\Delta\theta$  is

$$\Delta r = D_A \Delta\theta \approx 6 \left( \frac{H_0 D_A}{0.4} \right) \left( \frac{\Delta\theta}{1''} \right) h^{-1} \text{kpc}. \quad (9)$$

Note that for  $z = 1 - 3.5$ ,  $H_0 D_A$  is almost constant at 0.4 in a cosmology near the concordance model. Image separations tend to be in the 1–5'' range. For such transverse separations, much smaller than the gas Jeans scale of  $\sim 300 h^{-1}$  kpc, the Lyman- $\alpha$  lines should be coherent in the multiple images (Peeples et al. 2010). Note that if we wanted to use very long time-delay systems (though few are known, none with  $\Delta t > 3$  y) then these tend to have larger image separations, roughly  $\Delta t \sim (\Delta\theta)^2$  and the coherence may be degraded for hypothetical systems with separations greater than tens of arcseconds.

Wide field surveys such as Dark Energy Survey and LSST will find approximately  $10^3$  and  $10^4$  strongly lensed quasars, respectively. Monitoring campaigns such as COSMOGRAIL (COSMOGRAIL 2014) and STRIDES (STRIDES 2014) obtain long term light curves for their images, measuring the time delays. Depending on the time delay, photometry quality, and other factors it may take up to 1000 nights to obtain a time delay estimation, though note that the accuracy requirements may be relaxed from the time delay distance case, e.g. 5% accuracy may be sufficient for this not to contribute significantly to the redshift drift uncertainty. The differential redshift measurement itself takes only a single night, so the story of the universe may be revealed in 1000 nights and a night (Burton 1885).

Note that by the nature of the strong lensing time delay, it may be possible to crosscalibrate the spectra in both space and time. That is, if the time delay between images A and B is one year, say, then if observing the system one year later the spectrum of image B should match that of image A from the previous year. This “time anchoring” may add some robustness to the spatial anchoring of observing multiple images of the same source simultaneously.

Lensing can affect the image redshifts if the lens is moving (Mitrofanov 1981; Birkinshaw & Gull 1983). From Eq. (3) we see this arises because the dot product between the photon four-momentum and the source and observer four-velocities has to go through the intermediate step of the lens plane,

where the deflection shifts the angle between the vectors. The redshift contribution is of order  $v \delta\alpha$ , where  $\delta\alpha \sim \psi$  is the deflection angle. The redshift drift contribution is then  $d(v \delta\alpha)/dt$ , much smaller than a standard peculiar acceleration of the source and so can be neglected.

If the propagating light is absorbed in the Lyman- $\alpha$  forest due to neutral hydrogen gas along the path, then many narrow spectral features arise, enabling multiple measurements of the redshift drift (Loeb 1998; Liske et al. 2008), also with time delays. Embedded within the image spectra are not only the source redshift but the redshifts of each Lyman- $\alpha$  absorber. Thus in a single night we get not only multiple images with cosmology-provided time delays, but multiple signals within each image spectrum. The  $N_{\text{line,q}}$  spectral lines in the quasar, perhaps  $\mathcal{O}(10^3)$ , help to improve the signal-to-noise by  $\sqrt{N_{\text{line,q}}}$  but moreover the  $N_{\text{line,f}}$  lines in the forest, also perhaps  $\mathcal{O}(10^3)$ , simultaneously applies the redshift drift test at multiple redshifts – with their individual  $\dot{z}(z)$  – potentially improving the cosmological model constraints as discussed in Sec. 2.

#### 4. Experimental Approaches for High-Precision Redshift Drift Measurements

In this section we turn from theoretical speculation to consideration of innovative experimental approaches, with practical details on how to obtain highly precise redshift measurements. To provide context, the redshift measurement with  $\sigma_z = 6 \times 10^{-7}$  obtained from the radio absorption line in 3C 286 at  $z = 0.849$  (Davis & May 1978) is representative of current high-precision work. We are guided by two concepts: that low-redshift measurements can have significant cosmological leverage, and simultaneous differential measurements can be more robust than individual, absolute measurements of redshift.

Traditionally, one might wavelength calibrate a spectrum with an external standard, such as an iodine cell, and then repeat this ten or so years later with the next redshift measurement of the source. However, the wavelength calibration is not guaranteed to remain fixed over this long time span; indeed Griest et al. (2010); Whitmore et al. (2010) find it can shift significantly over a single night with changes in temperature, humidity, etc.

These stability issues can be ameliorated with a simultaneous differential measurement.

##### 4.1. Emission Line Galaxies as Targets

Emission line galaxies are excellent candidates for the measurement of precision redshifts. The best sources involve bright, narrow lines that are clearly identifiable. The unique signature of doublets amidst other emission lines allows unambiguous identification of the [OII]  $\lambda\lambda 3727\text{--}3729\text{\AA}$  and [OIII]  $\lambda\lambda 4959\text{--}5007\text{\AA}$  doublets. Their high line fluxes provide strong signals that suppress statistical Poisson uncertainty. Doublets occupy only a narrow bandwidth that spectrographs must span; regions outside the doublet need not be measured. The two lines composing a doublet are produced by the same atoms and therefore share a common line profile: as the wavelength separation of the two lines is proportional to  $(1+z)$ , their cross-correlation in log-wavelength thus provides a measure of redshift that is independent of the specific shape of the line profile.

The true functional forms of the line profiles are a priori unknown, which can lead to redshift uncertainty. Quoted line effective-wavelength uncertainties are generally up to a factor 10 finer than the resolution: for example a line with  $\Delta v = 3 \text{ km s}^{-1}$  is measured to precision  $\Delta\lambda/\lambda \gtrsim 10^{-6}$ . However, the redshift drift measurement does not require knowledge of the effective wavelength but rather only the wavelength shift of the profile, whatever the profile is. As just noted, within a single exposure the cross-correlation of the two doublet lines provides a robust redshift measurement. Similarly, cross-correlation of multiple spectra taken at different epochs provides a robust redshift-drift measurement.

We study potential targets from the Sloan Digital Sky Survey data release SDSS3 DR10. The Portsmouth Emission-Line Kinematics table (Thomas et al. 2013) is used to select objects with  $z > 0.08$  and sharp and bright [OII] and/or [OIII] emission lines. The redshifts, velocity dispersions  $\Delta v$ , line strengths, and host continuum levels for a select set of galaxies are shown in Table 2. The two-line average  $\Delta v$  for [OII], and the continuum fluxes for both doublets are given. The Portsmouth table gives “rest-frame” fluxes corrected for dust correction; the observed fluxes needed to simulate observations are taken from



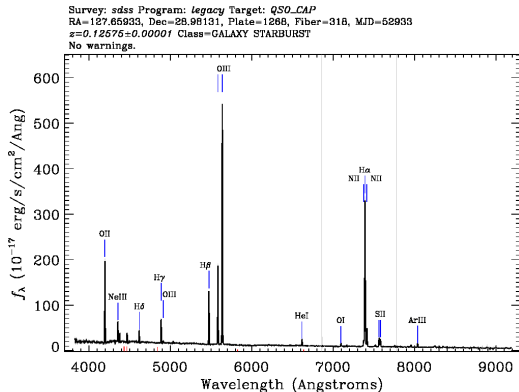


Fig. 5.— Spectrum of SDSS target specified by Plate #1268, Fiber #318 from the SDSS3 DR10.

the spZline data model (Bolton et al. 2012). In some cases only one doublet is visible, for example with high-redshift galaxies where [OIII] features are shifted to the near-infrared and are difficult to access from ground-based observations. The SDSS spectrum from a representative target, from Plate #1268, Fiber #318, is shown in Figure 5.

The tabulated galaxies are not the product of an exhaustive search and are meant to represent a minimum of what can be available as good candidate targets. Future surveys such as eBOSS, Dark Energy Spectroscopic Instrument, and Euclid will specifically target emission-line galaxies from which the best targets can be identified. (Also, emission line galaxies occur more in the field than in clusters, potentially ameliorating peculiar accelerations.) In the scenarios considered in this article, redshift precision scales linearly with the line width and the inverse square root of line flux, so bright, narrow lines are desired.

The spectral regions of interest are around each doublet. In the calculations that follow, these areas are modeled as a function of wavenumber  $\sigma$  as

$$B(\sigma) = \frac{a_1}{\sqrt{2\pi s_1^2}} \exp\left[-\frac{(\sigma - \sigma_1)^2}{2s_1^2}\right] + \frac{a_2}{\sqrt{2\pi s_2^2}} \exp\left[-\frac{(\sigma - \sigma_2)^2}{2s_2^2}\right]. \quad (10)$$

The two lines have central wavenumbers  $\sigma_1$  and  $\sigma_2$ , and share a common Gaussian profile with

width parametrized by velocity dispersion such that  $s_i = \sigma_i \Delta v / c$  and  $\Delta v$  is fixed for each galaxy.

## 4.2. Spectrograph Types for Measurements

The precision with which redshift can be determined depends on the instrument used for the measurement. We consider several spectrometers designs, including a “Conventional” high-resolution dispersion spectrograph and the interferometric instruments “EDI”, “SHS”, and “ED-SHS” described in the following subsections. Interferometers produce a Fourier transform of a signal, converting sharp spectral features into wave patterns whose frequency is dependent on the feature wavelength. Interferometers provide increased statistical sensitivity to wavelength measurements and potentially have less sensitivity to systematic uncertainties.

Some common assumptions are made for our analysis of spectrometer measurements. The baseline observation is for an 8-hour exposure on a 10-m telescope. To allow direct comparison of the designs, all systems are assigned the same total throughput of 70%. The dispersion spectrometer used for Conventional, EDI, and ED-SHS instruments is taken to have resolution  $R = 20000$  with a point-spread-function dominated by the pixel top-hat function. For all cases considered the photon noise will dominate uncertainties; nevertheless we include a detector read noise of  $2e^-$ , total integrations split into 2-hour exposures, and a dark current of  $2e^- s^{-1}$ . Blocking filters remove flux in wavelengths outside the regions of interest. The new moon CTIO sky emission is included and is small compared to the galaxy continuum. Spatial information is unimportant and the target is considered as point-like: a circular aperture of  $1''$  diameter is assumed to cover the full line flux. The effective PSF (including pixels and possible sub-pixel quantum efficiency variation) Nyquist samples the intrinsic line profiles. When appropriate, the sampling along the spatial axis is not included explicitly in the signal equations for conciseness.

Projected redshift precisions are calculated with Fisher matrix analysis with the source redshift  $z$  as the only free parameter. Precisions scale as the inverse square root of exposure time and inverse of telescope aperture. For the SHS, and when the other spectrographs resolve the spec-

TABLE 2  
TARGET LINE PROPERTIES.

Plate	Fiber	$z$	Doublet	$\Delta v$ ( $\text{km s}^{-1}$ )	Flux 1 ( $\text{erg s}^{-1}\text{cm}^{-2}$ )	Flux 2 ( $\text{erg s}^{-1}\text{cm}^{-2}$ )	Continuum ( $\text{erg s}^{-1}\text{cm}^{-2}\text{\AA}^{-1}$ )
1523	602	0.089	[OIII]	5.14	$7.04 \times 10^{-16}$	$2.13 \times 10^{-15}$	$1.97 \times 10^{-17}$
1935	204	0.098	[OII]	10.054	$1.06 \times 10^{-14}$	$1.28 \times 10^{-14}$	$2.39 \times 10^{-16}$
			[OIII]	10.04	$1.96 \times 10^{-14}$	$5.93 \times 10^{-14}$	$1.92 \times 10^{-16}$
1036	584	0.108	[OIII]	4.55	$3.47 \times 10^{-16}$	$1.05 \times 10^{-15}$	$4.42 \times 10^{-17}$
2959	354	0.120	[OIII]	6.86	$1.11 \times 10^{-16}$	$3.36 \times 10^{-16}$	$1.51 \times 10^{-18}$
1268	318	0.126	[OII]	10.044	$5.89 \times 10^{-15}$	$6.29 \times 10^{-15}$	$1.77 \times 10^{-16}$
			[OIII]	10.04	$1.09 \times 10^{-14}$	$3.32 \times 10^{-14}$	$1.46 \times 10^{-16}$
1657	483	0.221	[OII]	10.359	$4.69 \times 10^{-15}$	$4.28 \times 10^{-15}$	$1.36 \times 10^{-16}$
			[OIII]	10.30	$6.07 \times 10^{-15}$	$1.84 \times 10^{-14}$	$1.09 \times 10^{-16}$
1073	225	0.272	[OII]	84.746	$8.38 \times 10^{-16}$	$1.05 \times 10^{-15}$	$3.36 \times 10^{-17}$
			[OIII]	1.43	$3.75 \times 10^{-16}$	$1.14 \times 10^{-15}$	$3.89 \times 10^{-17}$
1514	137	0.318	[OII]	10.005	$1.20 \times 10^{-15}$	$1.74 \times 10^{-15}$	$6.35 \times 10^{-17}$
			[OIII]	10.01	$3.85 \times 10^{-16}$	$1.17 \times 10^{-15}$	$1.07 \times 10^{-16}$
4794	757	0.560	[OII]	45.890	$2.03 \times 10^{-16}$	$3.18 \times 10^{-16}$	$8.18 \times 10^{-18}$
			[OIII]	26.45	$8.29 \times 10^{-17}$	$2.51 \times 10^{-16}$	$1.51 \times 10^{-17}$
1059	564	0.693	[OII]	9.580	$1.40 \times 10^{-17}$	$1.94 \times 10^{-14}$	$1.47 \times 10^{-17}$

tral line, the precision scales inversely with the line dispersion velocity. As the measurements are source-noise dominated, redshift precisions scale as the inverse square root of line flux.

We are interested in uncertainties in redshift drift. This is in some ways simpler than measuring absolute redshifts because correlated redshift uncertainties cancel each other when measuring drift. Instruments contribute sources of measurement uncertainty in redshift drift through uncertainty in the conversion from pixel counts to physical flux, uncertainty in the point spread function, and limitations in the calibration of wavelength. These uncertainties distort intrinsic line shapes and so introduce error in the cross-correlation of the doublet lines and spectra taken on different dates. Each spectrograph type has different susceptibilities to systematic uncertainties.

### 4.3. Conventional Dispersion Spectrograph

The redshift of a galaxy can be measured from the output of a dispersion spectrograph, such as shown in Figure 5. For an input spectrum  $B(\sigma)$

the expected signal is

$$I(\sigma) = [B(\sigma) \otimes \text{PSF}(\sigma)] \text{III} \left( \frac{\sigma}{p} \right), \quad (11)$$

where  $p$  is the spacing of the wavenumber sampling and the Shah function  $\text{III}$  is the set of delta functions that specify the discrete sampling,

The wavelengths of the observed lines are compared to the corresponding known restframe to give the redshift. Projected statistical uncertainties from an  $R = 20000$  spectrograph for the target galaxies are given under the ‘‘Conventional’’ column of Table 3. Results from [OII], [OIII], and their combination are listed separately.

Not included in Table 3 are sources of instrumental systematics. Wavelength calibration is performed through observations of arc lamps emitting lines at known wavelengths. The line density is sparse, in that an arc line is not placed on every detector pixel. If the arc is taken simultaneously with the science exposure, a minimum wavelength interpolation distance must be maintained so that the arc does not interfere with the doublet. Otherwise, the arc must be observed in a different exposure. Therefore, temporal and/or wavelength

TABLE 3

STATISTICAL REDSHIFT UNCERTAINTIES OF SELECT SDSS TARGETS WITH AN 8 HOUR EXPOSURE ON A 10-M TELESCOPE FOR DIFFERENT SPECTROGRAPH TYPES.

Plate	Fiber	Doublet	Conventional	EDI	SHS	ED-SHS
1523	602	OIII	$1.7 \times 10^{-8}$	$5.8 \times 10^{-9}$	$2.4 \times 10^{-8}$	$5.9 \times 10^{-9}$
1935	204	OII	$1.4 \times 10^{-8}$	$4.4 \times 10^{-9}$	$1.7 \times 10^{-8}$	$4.5 \times 10^{-9}$
		OIII	$6.3 \times 10^{-9}$	$2.0 \times 10^{-9}$	$7.9 \times 10^{-9}$	$2.0 \times 10^{-9}$
		OII&OIII	$5.7 \times 10^{-9}$	$1.9 \times 10^{-9}$	$7.2 \times 10^{-9}$	$1.9 \times 10^{-9}$
1036	584	OIII	$2.3 \times 10^{-8}$	$7.7 \times 10^{-9}$	$4.2 \times 10^{-8}$	$7.8 \times 10^{-9}$
2959	354	OIII	$6.0 \times 10^{-8}$	$2.0 \times 10^{-8}$	$9.5 \times 10^{-8}$	$2.1 \times 10^{-8}$
1268	318	OII	$1.9 \times 10^{-8}$	$6.3 \times 10^{-9}$	$2.5 \times 10^{-8}$	$6.4 \times 10^{-9}$
		OIII	$8.6 \times 10^{-9}$	$2.8 \times 10^{-9}$	$1.1 \times 10^{-8}$	$2.8 \times 10^{-9}$
		OII&OIII	$7.9 \times 10^{-9}$	$2.5 \times 10^{-9}$	$1.0 \times 10^{-8}$	$2.5 \times 10^{-9}$
1657	483	OII	$2.4 \times 10^{-8}$	$7.9 \times 10^{-9}$	$3.1 \times 10^{-8}$	$8.0 \times 10^{-9}$
		OIII	$1.2 \times 10^{-8}$	$4.0 \times 10^{-9}$	$1.6 \times 10^{-8}$	$4.0 \times 10^{-9}$
		OII&OIII	$1.1 \times 10^{-8}$	$3.6 \times 10^{-9}$	$1.4 \times 10^{-8}$	$3.6 \times 10^{-9}$
1073	225	OII	$7.2 \times 10^{-7}$	$2.3 \times 10^{-7}$	$8.7 \times 10^{-7}$	$2.3 \times 10^{-7}$
		OIII	$1.2 \times 10^{-8}$	$4.4 \times 10^{-9}$	$1.3 \times 10^{-8}$	$5.1 \times 10^{-9}$
		OII&OIII	$1.2 \times 10^{-8}$	$4.4 \times 10^{-9}$	$1.3 \times 10^{-8}$	$5.1 \times 10^{-9}$
1514	137	OII	$4.3 \times 10^{-8}$	$1.4 \times 10^{-8}$	$5.5 \times 10^{-8}$	$1.4 \times 10^{-8}$
		OIII	$5.6 \times 10^{-8}$	$1.8 \times 10^{-8}$	$1.3 \times 10^{-7}$	$1.8 \times 10^{-8}$
		OII&OIII	$3.4 \times 10^{-8}$	$1.1 \times 10^{-8}$	$5.1 \times 10^{-8}$	$1.1 \times 10^{-8}$
4794	757	OII	$6.2 \times 10^{-7}$	$1.9 \times 10^{-7}$	$6.6 \times 10^{-7}$	$2.0 \times 10^{-7}$
		OIII	$4.1 \times 10^{-7}$	$1.3 \times 10^{-7}$	$9.0 \times 10^{-7}$	$1.3 \times 10^{-7}$
		OII&OIII	$3.4 \times 10^{-7}$	$1.1 \times 10^{-7}$	$5.3 \times 10^{-7}$	$1.1 \times 10^{-7}$
1059	564	OII	$1.7 \times 10^{-8}$	$5.6 \times 10^{-9}$	$1.6 \times 10^{-8}$	$5.6 \times 10^{-9}$

interpolation are applied to calibrate wavelengths.

The small number of pixels measuring line flux places stringent requirements on flatfield calibration. The FWHM of a  $10 \text{ km s}^{-1}$  feature is spanned by 3.15 pixels along the dispersion axis, and (for our calculations) 3 pixels along the spatial axis. A single pixel covered by one of the [OIII] lines of the SDSS target specified by Plate #1268, Fiber #318 has  $\sim 10^6$  counts; in order for photon noise to dominate over pixel flux uncertainty the calibration must be done to significantly better than 0.1%.

Uncertainty in the often variable and charge-dependent point spread function can bias the determination of the line centroids. Just as with the flux calibration requirement, sub-per-mil accuracy in predicted pixel counts is required. For redshift drift, these calibration requirements are differential between observations taken over the duration of the survey: if absolute calibration is not achieved, instrumental stability is essential.

#### 4.4. Externally Dispersed Interferometer

The Externally Dispersed Interferometer (EDI; Erskine 2003) is a candidate instrument to measure precision redshifts. An EDI is the sequence of a Fourier transform spectrograph (FTS) and a dispersion spectrograph. The FTS is an interferometer that shifts the phase of incoming coherent light by an amount dependent on wavelength and a delay between the two arm lengths. The ensuing dispersion spectrograph takes the phased light and separates it into fine wavelength bins. For an individual wavelength bin the output signal depends on the phase introduced by the interferometer; multiple measurements taken after dithering the delay make apparent a modulation in the output signals. Therefore, in an EDI the wavelength can be measured using both the calibration methods of a standard dispersion spectrograph *and* from the modulations of signal apparent when changing the FTS arm-lengths. As a consequence, it was shown by Erskine (2003) that EDI's provide line-velocity measurements that are more precise than with a dispersion spectrograph.

An EDI produces measurements that can be related to a conventional spectrum

$$I(\sigma) = B(\sigma) \otimes \text{PSF}(\sigma), \quad (12)$$

and an independently measurable whirl

$$W(\sigma) = \frac{1}{2} [e^{i2\pi\tau\sigma} B(\sigma)] \otimes \text{PSF}(\sigma), \quad (13)$$

where  $B$  is the input spectrum,  $\tau$  is the interferometer delay with units of distance, and PSF is the blurring response of a pure frequency.

The heterodyning feature of the EDI is seen in the Fourier transforms of the above expressions:

$$\begin{aligned} i(\rho) &= b(\rho) \text{psf}(\rho) & (14) \\ w(\rho - \tau) &= \frac{1}{2} b(\rho) \text{psf}(\rho - \tau). & (15) \end{aligned}$$

The EDI whirl has the instrumental frequency response shifted into a new  $\rho$  range to allow spectral resolution on scales tuned by the choice of  $\tau$ . In the calculations that follow, the delay is chosen to resolve the FWHM of the line with the lower wavenumber,  $\tau = (2.36s_1)^{-1}$ , where  $s_1$  was introduced in Eq. 10 as the standard deviation width of the first line.

An EDI observation is actually a series of measurements

$$\begin{aligned} I(\sigma)_{\Delta\tau} &= [B(\sigma) (1 + \cos(2\pi(\tau + \Delta\tau)\sigma + \phi_y)) \\ &\otimes \text{PSF}(\sigma)] \text{III} \left( \frac{\sigma}{p} \right), \end{aligned} \quad (16)$$

where  $p$  is the spacing of the wavenumber sampling,  $\phi_y$  is the initial phase, and  $\Delta\tau$  represents the changes in delay in the series of exposures; for our calculations we choose  $\Delta\tau = (n/4)[2/(\sigma_1 + \sigma_2)]$  with  $n \in \{0, 1, 2, 3\}$ , achieved by adjusting an interferometer arm length by quarters of the inverse average wavenumber. (This choice for the set of  $\Delta\tau$  is made for mathematical convenience and generally does not strongly affect the statistical determination of whirl.) The first term represents the signal obtained with a conventional spectrograph while the second, cosine term introduces a wavelength-dependent phase that provides additional leverage in measuring redshift.

The expected signal for one of the [OIII] lines of the SDSS target specified by Plate #1268, Fiber #318 is shown in Figure 6. In this case the nominal delay is  $\tau = 3.57 \text{ mm}$  with measurements made in steps of  $0.14 \mu\text{m}$ .

The redshift precisions on the target galaxies are given in Table 3, where each of the four phases

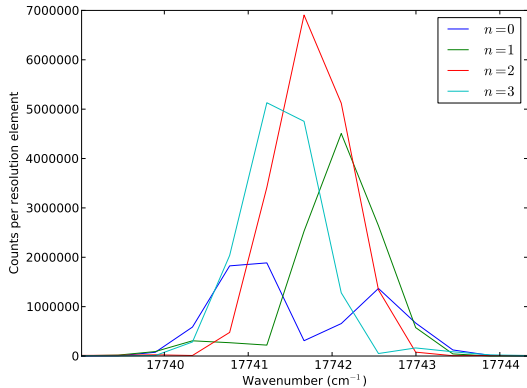


Fig. 6.— The expected EDI signal from the four phase measurements for one of the [OIII] lines of the SDSS target specified by Plate #1268, Fiber #318. The four phases parametrized by  $n$  are defined in Eq. 16.

receives a 2-hour exposure. The EDI performance includes that of the Conventional spectrograph plus the additional contribution from the whirl; in total the EDI outperforms the Conventional spectrograph in redshift precision by a factor of  $\sim 3$ .

Separating the EDI information into Conventional and whirl contributions, the signal and constraint from the Conventional spectrograph contribution shares those same systematic uncertainties. The whirl component is best calibrated using arc lamps in the science exposure. The arc lines determine the configuration of the EDI itself,  $\phi_y$  and the  $\Delta\tau$ 's, and do not have to be close to the science lines. This avoids the temporal and wavelength interpolation needed in conventional spectrographs. Wavelength uncertainty would then come from mismeasurement of phase and frequency due to pixels local to the science lines, so absolute flux and PSF uncertainties become irrelevant.

PSF calibration is facilitated with the presence of arc lines from which the PSF of the science lines can be interpolated.

## 4.5. Spatial Heterodyne Spectroscopy

### 4.5.1. Measuring Redshift

Redshift can also be measured through the sum and the difference of observed wavenumbers of two

lines whose restframe wavenumbers are known:

$$1 + z = \frac{\sigma_{10} + \sigma_{20}}{\sigma_1 + \sigma_2} = \frac{\sigma_{10} - \sigma_{20}}{\sigma_1 - \sigma_2}, \quad (17)$$

where  $\sigma_i$  is the observed and  $\sigma_{i0}$  the restframe wavenumber of line  $i$ . At face value, the measurement of  $\sigma_1 \pm \sigma_2$  should be expected to suffer larger uncertainty than that of the wavenumber of a single line. To counter this expectation, we consider a scenario where the experimental setup has an output that is naturally sensitive to  $\sigma_1 \pm \sigma_2$ . The differential measurement can be immune to certain systematic uncertainties encountered when using dispersion spectrographs. Redshifts are measured from the relative shift of two lines of a doublet; the single line profile common to them enables cancellation of the PSF blurring of the line profiles.

### 4.5.2. Signal

We consider Spatial Heterodyne Spectroscopy (SHS) (Harlander & Roesler 1990) as a means to get a direct measurement of  $\sigma_1 \pm \sigma_2$ . Conceptually, the SHS can be understood as an interferometer with the mirrors replaced by diffraction gratings. (Practically we assume an interferometer configuration that avoids the 50% light loss inherent to Michelson interferometers.) The gratings have line-spacing  $d$  and both are tilted by  $\theta$  with respect to the optical axis. The deflected light from each grating exits the interferometer as a plane wave propagating with angle  $\gamma$  away from the optical axis, given by the grating equation

$$\sigma (\sin \theta + \sin (\theta - \gamma)) = m/d, \quad (18)$$

where  $\sigma$  is the wavenumber and  $m$  the diffraction order. The angle of the emergent wave can be re-expressed as

$$\begin{aligned} \sin \gamma = & -\cos \theta \left( \frac{m}{d\sigma} - \sin \theta \right) \\ & + \sin \theta \sqrt{1 - \left( \frac{m}{d\sigma} - \sin \theta \right)^2}, \end{aligned} \quad (19)$$

which is useful in calculations.

The two wavefronts from the two gratings, incident on the detector at angles  $-\gamma$  and  $\gamma$ , interfere to make a fringe pattern with frequency

$$f_x = 2\sigma \sin \gamma. \quad (20)$$

For an input spectrum  $B(\sigma)$ , the intensity seen at position  $x$  on the detector is

$$I(x) = \frac{1}{\Delta x} \left[ \int_0^\infty B(\sigma) (1 + \cos(2\pi x(2\sigma \sin \gamma))) d\sigma \otimes \text{PSF}(x) \right] \text{III} \left( \frac{x}{p} \right), \quad (21)$$

where  $p$  is the spacing of the wavenumber sampling, and for simplicity we assume a square collimated beam that covers a range  $\Delta x \gg (2\sigma \sin \gamma)^{-1}$ . Since each spectral component is modulated by a distinct spatial frequency at the output, the Fourier transform of  $I(x)$  will recover the input spectrum. The Littrow wavenumber  $\sigma_0$  is defined such that  $2\sigma_0 \sin \theta = m/d$ ,  $\gamma = 0$  and no fringe patterns are produced.

#### 4.5.3. Toy Example

For illustration, consider a toy example where the input signal consists of two  $\delta$ -functions with the same intensity

$$B(\sigma) = \delta(\sigma_1) + \delta(\sigma_2). \quad (22)$$

The output signal density in this case is

$$\begin{aligned} I(x) &= \frac{1}{\Delta x} [2 + \cos(2\pi(2\sigma_1 \sin \gamma_1)x) \\ &\quad + \cos(2\pi(2\sigma_2 \sin \gamma_2)x)] \\ &= \frac{2}{\Delta x} [1 + \cos(2\pi(\sigma_1 \sin \gamma_1 + \sigma_2 \sin \gamma_2)x) \\ &\quad \times \cos(2\pi(\sigma_1 \sin \gamma_1 - \sigma_2 \sin \gamma_2)x)]. \end{aligned} \quad (23)$$

The two mixing of the sinusoidal outputs of the two lines results in two beat frequencies ( $\sigma_1 \sin \gamma_1 \pm \sigma_2 \sin \gamma_2$ ).

When the SHS is configured such that the Littrow wavenumber is very close to  $\sigma_1$  and  $\sigma_2$  (and hence  $\gamma_1$  and  $\gamma_2$  are small),

$$\sigma_{1,2} \sin \gamma_{1,2} \approx 2(\sigma_{1,2} - \sigma_0) \tan \theta \quad (25)$$

and the beat frequencies can be expressed as  $2(\sigma_1 + \sigma_2 - 2\sigma_0) \tan \theta$  and  $2(\sigma_1 - \sigma_2) \tan \theta$ . Each beat frequency provides information on either  $\sigma_1 \pm \sigma_2$ , the two quantities that directly lead to redshift.

The ratio  $n$  between the beat frequencies can be chosen by adjusting the SHS configuration to give

$$\sigma_0 = \frac{\sigma_1 + \sigma_2}{2} - \frac{\sigma_1 - \sigma_2}{2n}. \quad (26)$$

For  $n = \infty$  the Littrow wavenumber is set to the average of the two lines:  $\sigma_0 = (\sigma_1 + \sigma_2)/2$  and the first beat frequency is zero, which in practice is difficult to quantify through measurement. When  $n = 1$  the Littrow wavenumber is  $\sigma_2$ , meaning that line produces a flat signal and the other is the source of the oscillations; the values of the two beat frequencies are equal.

#### 4.5.4. Performance on Target Galaxies

We calculate the expected signal using the first order  $m = 1$  for a SHS with grating line density  $1/d = 1200 \text{ mm}^{-1}$  and using the more realistic double line model of Eq. 10. Different configurations of the SHS are achieved by adjusting the grating tilt angle  $\theta$ , although swapping gratings can achieve a similar effect. The SHS configuration can then be expressed in terms of the Littrow wavenumber.

For the [OIII] doublet of the SDSS target specified by Plate #1268, Fiber #318 the condition for having only one beat frequency occurs when  $\sigma_0 = \sigma_2 = 17913 \text{ cm}^{-1}$  and occurs at  $\theta = 0.341551$  radians. Different choices of Littrow wavenumber produce different output signals: Figure 7 shows the expected counts adjusting  $\sigma_0$  to produce beat frequency ratios  $n = 1/3.5, 1/1.05, 1, 1.05, 3.5$  according to Eq. 26. The maximum  $x$  is chosen to be  $(12s_1 \tan \theta)^{-1}$  in order to cover the decay caused by the line-width. The effect on the signal of the choice of the beat frequency of  $2(\sigma_1 + \sigma_2 - 2\sigma_0) \tan \theta$  relative to the  $2(\sigma_1 - \sigma_2) \tan \theta$  frequency is clearly apparent. The precision is insensitive to the choice of  $\sigma_0$ , except for small deviations near  $n = 1$  and at integer ratios of the beat frequencies; we choose the case of  $n = 1.5$  or  $\theta = 0.3421194$  radians (a change in angle of  $1.95'$  from the  $n = 1$  case) as a representative example where the pixels resolve the frequencies of interest.

The redshift precisions on the target galaxies are given in Table 3. The statistical uncertainties are slightly worse than for the Conventional spectrograph and well below EDI. However, the results have reduced sensitivity to PSF uncertainties.

Wavelength calibration is tied to the determination of the SHS system parameters, the grating density  $1/d$  and angle  $\theta$ . Both can be calibrated externally through direct measurements, or arc lamp exposures; including lamp light in sci-

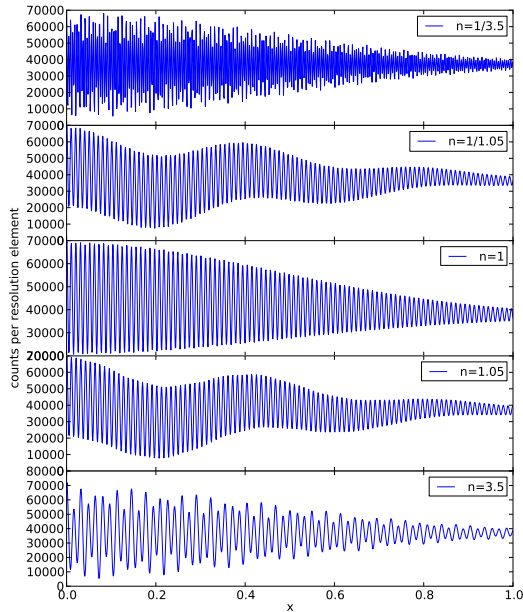


Fig. 7.— The output signal for positive  $x$  (it is symmetric about  $x = 0$ ) of five SHS configurations giving different Littrow numbers according to  $n = 1/3.5, 1/1.05, 1, 1.05, 3.5$  in Eq. 26.

ence exposures is not preferred as all sources of light contribute the noise background. Alternatively the long exposures can be divided into sub-exposures each with a different SHS configuration, either by changing the gratings or by rotating the grating angles by a series of  $\delta\theta$ . The data themselves can be then used to fit for the hardware parameters.

The line signal is distributed over thousands of pixels, reducing the pixel flux requirement to better than 1%, much less stringent than for the Conventional and EDI spectrographs.

Converting the spectrum to Fourier space transforms the sharp, imperfectly-known line profiles into the low-frequency envelope, distinct from the high-frequency wiggles characteristic to each configuration that inform the redshift measurement. The PSF blurring applies not in wavenumber space where it affects line shapes but rather in physical space after the conversion of the spectral lines into cosine functions.

#### 4.6. ED-SHS

The two doublet lines combine to produce a mixed signal in an SHS. Sending SHS light, such as those signals shown in Figure 7, into an ensuing dispersion grating allows the disentangling of the two signals for an unambiguous measurement of the frequency of each one. Here, this scheme is referred to as an External Dispersion SHS (ED-SHS). The observed signal is described by

$$I(\sigma, x) = \frac{1}{\Delta x} \left[ \int_{\sigma}^{\sigma} \exp(1/(2R)) d\sigma' B(\sigma') \right. \\ \left. \times (1 + \cos(2\pi x(2\sigma' \sin \gamma))) \right] \\ \otimes \text{PSF}(\sigma, x) \text{III} \left( \frac{\sigma}{p_{\sigma}} \right) \text{III} \left( \frac{x}{p_x} \right). \quad (27)$$

The similarities between ED-SHS and EDI can be seen in Fig. 2 of Erskine (2003); both use interferometry to create wavelength-dependent modulations in the signal, with the distinction between the two coming from the functional form of the modulation frequency.

The signal from two columns of pixels corresponding to the two wavelengths of the [OIII] doublet of the SDSS target specified by Plate #1268, Fiber #318 is shown in Figure 8. The Littrow wavelength is set to the average of the two lines  $\sigma_0 = (\sigma_1 + \sigma_2)/2$ . In an SHS the output signal would be the sum of these and all other columns in the bandpass.

The redshift precisions on the target galaxies are given in Table 3. The statistical uncertainties are improved compared to those of the SHS, and are comparable to the performance of the EDI.

Now that the signals from different wavelengths are no longer mixed, calibration arcs can be observed with the science image without increasing the photon noise of the doublet lines. Both wavelength and PSF calibration are simplified as with the EDI. In addition, the flux signals per pixel are further reduced relative to the SHS, relaxing flux calibration requirements.

## 5. Conclusions

Direct kinematic measurements of cosmic acceleration can provide valuable, model independent confirmation of dark energy. The accuracy

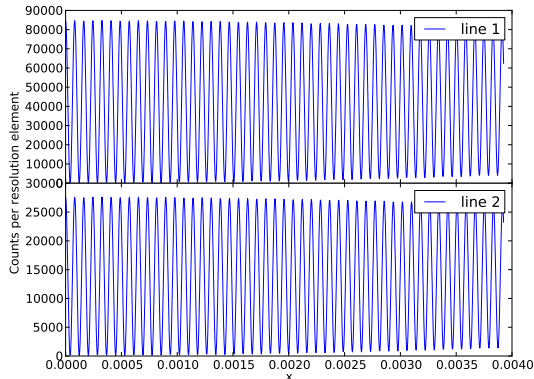


Fig. 8.— The output signal for positive  $x$  (it is symmetric about  $x = 0$ ) of the ED-SHS configuration with  $\sigma_0 = (\sigma_1 + \sigma_2)/2$ .

required for detecting redshift drift is challenging, and we have reviewed some of the systematics, presented a series of theoretical speculations for observational methods, and explored various promising improvements to experimental approaches to measuring directly spectral line shifts.

One surprising result is that the greatest leverage on dark energy properties comes from low-redshift observations, due to lesser covariances there with other cosmological parameters. The dark energy figure of merit can exceed 100 for a set of five measurements over  $z = [0.1 - 0.5]$ , each at 1% precision (together with current precision on the Hubble constant), i.e. determining  $w$  to 0.02,  $w_0$  to 0.06,  $w_a$  to 0.43. Moreover, redshift drift has extraordinary complementarity with other probes, having the opposite degeneracy in the  $w_0$ - $w_a$  plane from all standard probes. For example, combination of the low-redshift drift with Planck CMB data increases the figure of merit by a factor 12, to over 1000. Even a more practical 5% precision on redshift drift gives a FOM of 290 when combined with current Hubble constant and CMB data. Lesser complementarity can be achieved by combining redshift drift at low and high redshifts.

Given the potential leverage of redshift drift, and the ability for low redshift measurements to be powerful, we reconsider the “stare and wait” method of observing spectral lines from a high redshift source (or a series of sources in the Lyman- $\alpha$  forest) over a time span of decades. We specu-

late about three different concepts. The first measures Hubble drift rather than redshift drift per se, gives a complementary measure of acceleration, and can be accomplished with normal galaxy redshift survey data using differential radial baryon acoustic oscillations (drBAO). The second would use cosmic “pulsers”, not yet discovered, but possibly realizable through binary gravitational wave sources. Finally, long time-delay strong gravitational lenses, possibly to be detected by future deep time domain surveys, are also considered. We emphasize that these ideas are speculative and need considerable development, but do have considerable synergy with surveys already planned such as DESI, Euclid, and LSST. They can also replace patience – of several decade time scales, see the categorization of Stebbins (2012) – with ideas on how to get the universe and astrophysics to work for us.

More practically, we turn to experimental approaches for improving high precision redshift measurements. Given the leverage of low redshift we focus on bright emission line galaxies as targets. We explore three alternatives to conventional spectrographs, involving differential and interferometric methods, and calculate their signal-to-noise and potential redshift precisions. We find that single source redshift measurement precision of few  $\times 10^{-9}$  is potentially achievable, with further improvement possible from multiple sources, multnight exposures, and larger telescopes (our numbers are canonically for 8 hours on a 10-m telescope). “Gold” targets, with brighter and narrow doublet emission than the galaxies considered in this article, may yet be discovered in upcoming spectroscopic surveys and provide a speedier path toward detecting redshift drift. Instruments such as Externally Dispersed Interferometers and External Dispersion Spatial Heterodyne Spectroscopes can avoid some of the systematics in conventional spectrographs. Testing the stability and/or calibration precision possible on these instruments is of interest to see whether they can satisfy the requirements imposed by the science.

Other targets, such as narrow radio lines or sequences of lines from masers and molecular emission, should be explored, as should other uses of high-precision wavelength measurements, such as for atomic line catalogs.

Cosmic acceleration is a fundamental mystery



of physics, and the possibility of adding a new probe of it – one that is kinematic and does not depend on assumptions of how to separate matter and dark energy, or of their evolution – is an exciting prospect. The hardware and systematics will be highly challenging, but success means that we will open up a new time domain: the ability to watch the universe as it evolves in real time.

We acknowledge helpful discussions with Stephen Bailey, Jeff Newman, and Nao Suzuki. EVL thanks the Korea Astronomy and Space Science Institute for hospitality. This work has been supported by DOE grant DE-SC-0007867, by LLNL under Contract DE-AC52-07NA27344, and the Director, Office of Science, Office of High Energy Physics, of the U.S. Department of Energy under Contract No. DE-AC02-05CH11231.

## REFERENCES

- Birkinshaw, M., & Gull, S. F. 1983, *Nature*, 302, 315
- Bolton, A. S. et al. 2012, *AJ*, 144, 144, 1207.7326
- Burton, R. 1885, *The Book of the Thousand Nights and a Night*
- COSMOGRAIL. 2014, <http://www.cosmograil.org>
- Davis, M. M., & May, L. S. 1978, *ApJ*, 219, 1
- Erskine, D. J. 2003, *PASP*, 115, 255
- Fohlmeister, J., Kochanek, C. S., Falco, E. E., Morgan, C. W., & Wambsganss, J. 2008, *ApJ*, 676, 761, 0710.1634
- Fohlmeister, J. et al. 2007, *ApJ*, 662, 62
- Fohlmeister, J., Kochanek, C. S., Falco, E. E., Wambsganss, J., Oguri, M., & Dai, X. 2013, *ApJ*, 764, 186, 1207.5776
- Griest, K., Whitmore, J. B., Wolfe, A. M., Prochaska, J. X., Howk, J. C., & Marcy, G. W. 2010, *ApJ*, 708, 158, 0904.4725
- Harlander, J., & Roesler, F. L. 1990, in *Society of Photo-Optical Instrumentation Engineers (SPIE) Conference Series*, Vol. 1235, *Instrumentation in Astronomy VII*, ed. D. L. Crawford, 622–633
- Hojjati, A., Kim, A. G., & Linder, E. V. 2013, *Phys. Rev. D*, 87, 123512, 1304.0309
- Linder, E. V. 1997, *First Principles of Cosmology* (Prentice Hall)
- . 2010, *ArXiv e-prints*, 1004.4646
- Liske, J. et al. 2008, *MNRAS*, 386, 1192, 0802.1532
- Loeb, A. 1998, *ApJ*, 499, L111, astro-ph/9802122
- Lorimer, D. R. 2008, *Living Reviews in Relativity*, 11, 8, 0811.0762
- McVittie, G. C. 1962, *ApJ*, 136, 334
- Mitrofanov, I. G. 1981, *Soviet Astronomy Letters*, 7, 39
- Peebles, M. S., Weinberg, D. H., Davé, R., Fardal, M. A., & Katz, N. 2010, *MNRAS*, 404, 1295, 0910.0250
- Perlmutter, S. et al. 1999, *ApJ*, 517, 565, arXiv:astro-ph/9812133
- Riess, A. G. et al. 1998, *AJ*, 116, 1009, arXiv:astro-ph/9805201
- Sandage, A. 1962, *ApJ*, 136, 319
- Seikel, M., Clarkson, C., & Smith, M. 2012, *J. Cosmology Astropart. Phys.*, 6, 36, 1204.2832
- Shafieloo, A., Kim, A. G., & Linder, E. V. 2012, *Phys. Rev. D*, 85, 123530, 1204.2272
- Stebbins, A. 2012, *International Journal of Modern Physics D*, 21, 42017, 1205.4201
- STRIDES. 2014, private communication
- Tewes, M., Courbin, F., & Meylan, G. 2013, *A&A*, 553, A120, 1208.5598
- Thomas, D. et al. 2013, *MNRAS*, 431, 1383, 1207.6115
- Thornton, D. et al. 2013, *Science*, 341, 53, 1307.1628
- Treu, T. et al. 2013, *ArXiv e-prints*, 1306.1272
- Whitmore, J. B., Murphy, M. T., & Griest, K. 2010, *ApJ*, 723, 89, 1004.3325

Yunes, N., Pretorius, F., & Spergel, D. 2010,  
Phys. Rev. D, 81, 064018, 0912.2724